Supplementary Materials for

Discontinuous fibrous Bouligand architecture enabling formidable fracture-resistance with crack-orientation insensitivity

Kaijin Wu[1], Zhaoqiang Song[3], Shuaishuai Zhang[1], Yong Ni[1]*, Shengqiang Cai[3], Xinglong Gong[1], Linghui He[1], Shu-Hong Yu[2]

[1] *CAS Key Laboratory of Mechanical Behavior and Design of Materials, Department of Modern Mechanics,* CAS Center for Excellence in Complex System Mechanics, *University of Science and Technology of China, Hefei, Anhui 230026, China*

[2]*Division of Nanomaterials & Chemistry, Hefei National Laboratory for Physical Sciences at the Microscale, Department of Chemistry, Institute of Biomimetic Materials & Chemistry, University of Science and Technology of China, Hefei, Anhui 230026, China*

[3]*Department of Mechanical and Aerospace Engineering, University of California, San Diego, La Jolla, CA 92093, USA*

*Correspondence and requests for materials should be addressed to the author:
Yong Ni (yni@ustc.edu.cn).

This PDF file includes:

Supplementary Discussion 1: 3D printing fabrication and characterization of constituents

Supplementary Discussion 2: The details of fracture mechanics model

Supplementary Discussion 3: The effects of initial crack orientations.

Supplementary Discussion 4: The effects of twist angles distribution.

Supplementary Discussion 5: The fracture energy for crack bridging

Supplementary Discussion 6: Characterizations of the post-failure patterns in 3D-printed samples

Supplementary Discussion 7: Comparation between different bioinspired microstructures

Tables S1

Figures S1 to S11

Supplementary References

www.pnas.org/cgi/doi/10.1073/pnas.2000639117

Supplementary Discussion 1: 3D printing fabrication and characterization of constituents

The DFB composites were fabricated using multi-materials 3D-printing technology. The dimensions of the 3D-printed single-edge notched bend samples consisted of 25 layers are H = 22.5 mm, L = 5H, W = H, t = 0.9 mm, and h = H/5 with fiber diameter of 0.8 mm (Fig. 1*C*). The three-point bending coupons were 3D printed from designed CAD models by using an Objet260 Connex3 3D printer (Stratasys Ltd., USA), where the discontinuous fibers are made of a rigid polymer (VeroWhitePlus) and the matrix is made of a soft rubber-like polymer (TangoblackPlus). The dog-bone tensile specimens and three-points bending specimens were printed to characterize the mechanical properties of the polymers. The tensile specimen is characterized by a gauge dimension of 40 mm, a width of 5 mm and a thickness of 2 mm (Fig. S1*A* and S1*B*). A "rail-shear" dog-bone specimen is printed to characterize the shear performances of TangoblackPlus (Fig. S1*C*). The geometry of the rail is characterized by a length of 9 mm, a width of 3 mm and a thickness of 0.1 mm. In addition, the fracture toughness K_{Ic}^{f} of stiff fibers (VeroWhitePlus) was characterized using a three-point bending specimen as shown in Fig. S1*D*. The geometry the test specimen is characterized by a support span of 42 mm, a width of 10 mm, a thickness of 5 mm and an initial notch depth of 5 mm. All tests were carried out on a Material Test System (MTS criterion 43, MTS System Co., America) with constant displacement mode using 5 KN load cells at a loading rate of 0.5 mm/min. The fracture toughness K_{Ic}^{f} was calculated with the following equation:

$$K_{Ic}^{f} = \frac{P_{Ic}S}{BW^{3/2}} f(a/W) \tag{S1}$$

$$f(a/W) = \frac{3(a/W)^{1/2}[1.99-(a/W)(1-a/W)(2.15-3.93a/W+(a/W)^{2})]}{2(1+2a/W)(1-a/W)^{3/2}} \tag{S2}$$

where P_{Ic} is the maximum load value in the three-points bending tests.

Supplementary Discussion 2: The details of fracture mechanics model

We developed a fracture mechanics model for the discontinuous fibrous Bouligand (DFB) architrcture to consider the hybrid fracture modes with the combination of crack twisting and crack bridging. To simplify the analysis, we assumed that the model is based on linear elastic fracture mechanics with mode I loading. To characterize the helicoidal structure, a global coordinate system

(X, Y, and Z) of the domain is defined with the origin located at the middle of the initial flat crack front, X-axis is the axis at which the twisting crack front rotates, and Y-axis and Z-axis oriented along and perpendicular to the initial crack front orientation, respectively (Fig. S3*A*). In the meanwhile, the dimensionless coordinates are given by $\bar{X} = X / d, \bar{Y} = Y / d, \bar{Z} = Z / d$, where d is the fiber diameter. The DFB structure can be characterized by following parameters: the pitch angle γ_0 (the angle difference in orientation of adjacent fiber layer), dimensionless fiber length $\bar{l} = l / d$ (d is the fiber diameter) and twist angle distribution ϕ along the crack propagation direction (X-axis). With assuming that the continuous twisting crack is represented as a rotated flat plane with a straight crack front, the twist angle with linear distribution (constant pitch angle) along the X-axis can be expressed as:

$$\phi = \gamma_0 \bar{X} \tag{S3}$$

Based on the geometrical analysis on the characteristic of the twisting crack surface described in Fig. S3*A*, the tilted angle α can be expressed as:

$$\alpha = \tan^{-1}\left(\frac{d\bar{Z}}{d\bar{X}}\right) \tag{S4}$$

Because the continuous twisting surface is described by a twisting surface with a straight front, the crack shape in a rotation of 180° of the DFB structure can be described by

$$\bar{Z} = \bar{Y}\tan\left(\phi\left(\bar{X}\right)\right), 0 \le \bar{X} \le \pi / \gamma_0, -\bar{l}/2 \le \bar{Y} \le \bar{l}/2 \tag{S5}$$

With the assumption that the local coordinates systems (x, y, z) at the straight crack front of the twist flat plane remains identical, the local stress intensity factors (k_1', k_2', k_3') are then obtained by transforming the local stress field of kinked crack onto the twisted plane by a twisted angle ϕ (1, 2):

$$\begin{aligned}
k_1' / K_I^0 &= \cos^2\left(\frac{\alpha}{2}\right)\left\{2\nu\sin^2\phi + \cos^2\left(\frac{\alpha}{2}\right)\cos^2\phi\left[1 + 2\sin^2\left(\frac{\alpha}{2}\right)\right]\right\} \\
k_2' / K_I^0 &= -2\sin^3\left(\frac{\alpha}{2}\right)\cos^3\left(\frac{\alpha}{2}\right)\cos\phi \\
k_3' / K_I^0 &= -\cos^2\left(\frac{\alpha}{2}\right)\sin\phi\cos\phi\left\{2\nu - \cos^2\left(\frac{\alpha}{2}\right)\left[1 + 2\sin^2\left(\frac{\alpha}{2}\right)\right]\right\}
\end{aligned} \tag{S6}$$

where K_I^0 is the global applied stress intensity factor of mode I fracture, ν is Poisson's ratio (ν =

0.3).

Based on the local stress intensity factor, the local energy release rate of the twist crack G_t can be calculated by

$$G_t = \frac{1}{E}[k_1'^2(1-v^2) + k_2'^2(1-v^2) + k_3'^2(1+v)] \tag{S7}$$

where E is the Young's modulus. The normalized local energy release rate with crack titling is defined as $\bar{G}_t = G_t / G_0$, where $G_0 = \left(1-v^2\right)\left(K_I^0\right)^2 / E$ is the global energy release rate.

Considering the steady-state crack propagation with crack twisting, the local energy release rate G_t equals the intrinsic fracture energy Γ_{int}, which is taken as the energy dissipated by the breakage of matrix material, and the fracture energy G_t^c of the composite equals to the global energy release rate G_0 of the system, namely:

$$G_t^c = \Gamma_{\text{int}} \frac{G_0}{G_t} = \frac{\Gamma_{\text{int}}}{\bar{G}_t} \tag{S8}$$

When the twisted crack propagates to the direction almost parallel to the loading direction, its local energy release rate reduces dramatically and is too small to drive further crack propagation along the fiber alignment. As a result, the crack propagates cross the fibers to form crack bridging zone. Based on the crack bridging model (3, 4) shown in Fig. S3*B*, the global stress intensity factor K_I^0 of the composite with crack bridging can be written as

$$K_I^0 = K_I^{\text{int}} + K_I^b \tag{S9}$$

where K_I^{int} is the intrinsic fracture toughness of the matrix materials, and K_I^b denotes the stress intensity factor induced by the bridging stress, which can be calculated by (3)

$$K_I^b = \sqrt{2/\pi}\int_0^{\lambda}[\sigma_b(x)/\sqrt{\lambda - x}]dx \tag{S10}$$

where λ is the length of the crack-bridging zone, and σ_b is the bridging stress.

Further, the toughening ratio introduced by crack bridging at the stage of steady-state crack propagation is calculated as (4, 5):

$$\eta = K_I^b / K_I^{\text{int}} \tag{S11}$$

where η is a function of fiber length l, volume fracture of fiber V_f, fiber modulus E, fiber diameter d, interfacial strength τ_m and fracture toughness of fibers K_{Ic}^f, i.e., $\eta = 7.6 - 7.1\exp(-\Phi / 68.25)$, where the dimensionless parameter Φ is $\Phi = V_f \tau_m E l^2 / \left(\left(K_{Ic}^f \right)^2 d \right)$.

The local energy release rate of crack bridging at the stage of steady-state crack propagation could be given by

$$G_b = \frac{(1-\nu^2)(K_I^{\text{int}})^2}{E} = \frac{1}{(1+\eta)^2} G_0 \tag{S12}$$

where $G_0 = \left(1-\nu^2\right)\left(K_I^0\right)^2 / E$ is the energy release rate determined by the remote loading. The normalized local energy release rate is $\bar{G}_b = G_b / G_0$.

The fracture energy of crack bridging is given by

$$G_b^c = \Gamma_{\text{int}} \frac{G_0}{G_b} = (1+\eta)^2 \Gamma_{\text{int}} \tag{S13}$$

where Γ_{int} is the intrinsic fracture energy, and the normalized fracture energy is $\bar{G}_b^c = G_b^c / \Gamma_{\text{int}}$.

Based on the maximum energy release rate fracture criterion, the local energy release rate in the DFB structure can be calculated as

$$G = \max\left(G_t, G_b\right) \tag{S14}$$

Considering both the crack shape and local energy release rate, the effective normalized energy release rate with respect to the area of the undeflected crack plane can be given by (1)

$$\bar{G}_e = \frac{1}{S_0} \int_{S_0} \frac{G}{G_0} \cos\theta dS_0 = \frac{\gamma_0}{\pi \bar{l}} \int_{-0.5\bar{l}}^{0.5\bar{l}} \int_0^{\pi/\gamma_0} \frac{G}{G_0} \cos\theta dx dy \tag{S15}$$

where S_0 is the area of undeflected crack plane, and θ is the kinking angle between the normal to the deflected crack plane and the normal to the undeflected crack plane. At the stage of steady-state crack propagation, the local energy release rate G must equal to the intrinsic fracture energy Γ_{int}, so the effective fracture energy is given by

$$G_e^c = \Gamma_{\text{int}} / \bar{G}_e \tag{S16}$$

Therefore, the dimensionless effective fracture energy is $\bar{G}_e^c = G_e^c / \Gamma_{\text{int}}$. And the released strain

energy $\bar{U}$ in the crack-bridging zone $\bar{U}_b$ and that in the crack-twisting zone $\bar{U}_t$ can be calculated by the integration of the local energy release rate and crack area

$$\bar{U}_t = \int_{\bar{S}_t} \bar{G}_t d\bar{S}_t, \quad \bar{U}_b = \int_{\bar{S}_b} \bar{G}_b d\bar{S}_b \tag{S17}$$

where $\bar{S}_t$ is the area of the crack-twisting zone, and $\bar{S}_b$ is the area of the crack-bridging zone.

Supplementary Discussion 3: The effects of initial crack orientations.

With the consideration of the crack orientation β shown in Fig. S3*C*, where β is the angle between the axis of initial fiber layer at notch tip and direction of the notch front (Y-axis)), the twist angle distribution along the X-axis can be expressed as:

$$\phi = \gamma_0 \bar{X} + \beta \tag{S18}$$

The crack surface geometry and localized energy release rate distribution can be calculated based on equations (S5) and (S14). When the initial crack orientation is $\beta = \beta_0 \neq 0$ and the local energy release rate of crack twisting at $X = 0$ is less than the local energy release rate of crack bridging (i.e., $\bar{G}_t(\bar{X} = 0) < \bar{G}_b$), the crack at $X = 0$ will propagations with the mode of crack bridging ($\bar{G}(\bar{X} = 0) = \bar{G}_b$), and the geometry of the crack surface at $\bar{X} = 0$ in the structure with initial crack orientation $\beta = \beta_0 \neq 0$ is the same as the geometry of the crack surface at $\bar{X} = \beta_0 / \gamma_0$ in the structure with $\beta = 0$. Further, the effective fracture energy of the DFB structure under different initial crack orientations can be calculated based on equation (S16).

Supplementary Discussion 4: The effects of twist angles distribution.

To analyse the effects of the twist angles distribution ϕ in a pitch on the effective fracture energy, we designed the DFB structure with twist angles distributions described by a power function:

$$\phi = \frac{\gamma_0^n}{\pi^{n-1}} \bar{X}^n, \ \frac{1}{2} \le n \le 2 \tag{S19}$$

where $n = 1$ represents linear distribution of twist angle along the crack propagation direction (X-axis), i.e., the pitch angle in a pitch is constant, $0.5 \le n < 1$ represents nonlinear convex function distribution of twist angle and $1 < n \le 2$ represents nonlinear concave function distribution of twist

angle, as shown in Fig. S5*A*. The crack surface geometry, localized energy release rate distribution and effective fracture energy in the DFB structure with nonlinear distributions can be calculated based on equations (S5), (S14) and (S16).

Our calculated results show that the distribution forms of the twist angles affect the crack surface morphologies and the values of local energy release rate. The nonlinear twist angle distribution described by concave power function ($1 < n \leq 2$) results in that the crack bridging occurs far from the initial crack (Fig.S5*B*). For the Bouligand layups with nonlinear twist angle distribution described by convex power function ($0.5 \leq n < 1$), the transition from crack twisting to crack bridging occurs at the zone near initial crack (Fig.S5*C*). The twist crack surface area of the structure with nonlinear twist angles distribution becomes smaller than that of the structure with linear twist angle distribution, which leads to that the effective fracture energy at system with nonlinear twist angles distribution is lower than that in the system with linear twist angles distribution (Fig. S5*D*). For the DFB composites with nonlinear twist angles distribution, there also exists critical pitch angles and fiber size effects corresponding to maximum fracture energy. As shown in Fig. S5*E* and Fig. S5*F*, the optimized effective fracture energy $\bar{G}_e^c$ can be achieved through tuning the pitch angles γ_0 and fiber length $\bar{l}$ under nonlinear twist angles distribution. Further, the three-points bending tests revealed that there also exists optimal pitch angles and fiber size effects in the 3D-printed DFB samples with nonlinear twist angle distributions, and the structures with linear twist angles distribution (i.e., constant pitch angle) show higher total energy dissipation (Fig. S6). The experimental results are in good agreement with the theoretical results. Therefore, the above analyses illustrate the underlying mechanism for why the pitch angle in a pitch is constant in the natural materials with Bouligand structure and provide some structural design strategies for gradient materials.

Supplementary Discussion 5: The fracture energy for crack bridging

The material parameters for 3D-printed DFB samples, the natural beetle's exoskeleton containing chitin-protein fibers and the twisted cellulose fibrous composites (6-10) are listed in Table S1. The material parameters of the fiber phase and matrix phase in the 3D-printed DFB samples are obtained by three-points bending tests and tension tests, respectively, as shown in Fig. S1*A*-*D*. Based on the above parameters, we can calculated the fracture energy of crack bridging in the 3D-printed

DFB samples, beetle's exoskeleton containing chitin-protein fibers and twisted cellulose fibrous composites using the equations (S11) and (S13). The dimensionless fracture energy of crack bridging in 3D-printed DFB samples is $\overline{G}_b^c \approx 2.5$. The fracture energy of crack bridging in exoskeleton of beetles is $\overline{G}_b^c \approx 2.41$. The fracture energy of crack bridging for twisted cellulose composites is about $\overline{G}_b^c \approx 2.62$.

Supplementary Discussion 6: Characterizations of the post-failure patterns in 3D-printed samples

The area of the crack-twisting zone and crack-bridging zone were measured by ruler based on the distinct post-failure patterns of experiment samples, respectively. The crack bridging zone shows lots of fiber fracture or pull-out, where the failure occurs by separation of columnar stacks of fibers (nacre-like) oriented nearly parallelly to the loading direction. The crack twisting zone shows a twisting fracture paths that follow the spinning of fibers, i.e., the crack surface propagated through the fiber-matrix interface without breaking any fiber. For simplicity, the profile of the crack bridging zone is fitted by a planar quadrilateral, as shown in Figure S7. The distance of crack propagation in crack-bridging zone ($\overline{X}_b$) and the width of specimens (W) were measured by a ruler. Then, the dimensionless area of the crack twisting zone ($\overline{S}_b = W \cdot X_b / d^2$) can be obtained experimentally based on above space geometrical profiles. For crack twisting zone, the twisted crack shapes can be obtained by marking the exact fibers at the twisting crack surface from the fractured specimens. As shown in Figure S7, the twisting fracture surface can also be characterized through an analytical equation, $\overline{Z} = \overline{Y}\tan(\overline{X} \cdot \gamma_0),\ 0 \le \overline{X} \le X_t / d$, where $\overline{X} = X / d, \overline{Y} = Y / d, \overline{Z} = Z / d$ denote the distance along each axis with the origin of the coordinate system located at the center of the notch front, and the distance of crack propagation in crack-twisting zone ($\overline{X}_t$) can be measured by a ruler in experiments. Then, the dimensionless area of the crack twisting zone ($\overline{S}_t$) can be obtained experimentally based on above space geometrical profiles, and at least three samples were measured for each data to identify the area precisely.

Supplementary Discussion 7: Comparation between different bioinspired microstructures

To reveal the excellent mechanical performances of DFB architecture, five architectures have

been investigated experimentally, including hard-bulk structure, nacre-like structure, cross-lamellar structure, continuous fibrous Bouligand (CFB) architecture, and DFB architecture. For simplicity, all bricks are assumed to have the same size and are arranged periodically in nacre-like model, and the cross-lamellar model is adopted from Gu et al.'s work (11) for comparison. The geometric parameters for cross-lamellar structure are a = 2.8 mm, b = 2.5 mm, c = 2.9 mm and t = 0.25 mm; The geometric parameters for nacre-like structure are a = 0.8 mm, b = 2.4 mm, and t = 0.25 mm; The geometric parameters for CFB structure are d = 0.8 mm and t = 0.1 mm. These architectures are then 3D printed into three-point bending specimens with a same size using a commercial Objet Connex260 3D printer (Stratasys corporation). Considering the fiber-matrix material diffusion during the printing process due to the printer resolution limitations, the real volume fractions of the stiff phase for all architectures are about 70%. These three-point bending specimens were tested under same loading conditions.

We have constructed an Ashby diagram of the fracture energy dissipation and the maximum force for the 3D-printed specimens with DFB architecture and other architectures, as shown in Fig. S8 and Fig. S9. Compared with other typical architectures, the DFB architecture with optimized pitch angle exhibits the highest work of fracture (7-8 times improvement than the hard phase) due to a hybrid crack-twisting and crack-bridging mechanism. In Fig.S9, the nacre-like structure exhibits a stair-like force-displacement curve due to the pull-out and fracture of bricks and shows work of fracture improved by 4-5 times. Compared to the above structures, the cross-lamellar structures show relatively small toughness improvements (2-3 times) due to that the single crack is confined to the interface in the cross-lamellar structures with a pre-crack under three-point bending, corresponding to a relatively small fracture processing zone. It's worth mentioning that if the cross-lamellar specimens without a pre-crack is loaded under dynamic impact load, multiple cracks may initiation and more significant toughness improvement may be envisioned, which is consistent with the results in Gu et al.'s work (11). Further, the DFB structure with a critical pitch angle of about 20° exhibits the maximum fracture energy that is 3-4 times higher than that of the DFB structure with $\gamma_0 = 0^\circ$. Although the absolute value of the fracture work in DFB structure is not a significant improvement due to the limitation of the spatial resolution of 3D-printing technology and available 3D-printing polymer materials, both our fracture mechanics analyses and experiments confirm that the DFB structure with a critical pitch angle exhibits the maximum fracture energy that is 3-4 times higher

than the DFB structure with $\gamma_0 = 0^\circ$. Our results demonstrate that the DFB architecture with a specific pitch angle provides an example to significantly improve the effective fracture work of biomimetic composites.

In the meanwhile, the work of fracture in the cross-ply structures with pitch angle of $\gamma_0 = 90^\circ$ is about 3-4 times greater than the hard phase, due to that only half of the fibers in whole structure carry loads. Compared to the DFT structure with an optimized pitch angle, the CFB structures exhibit relatively low toughness improvements (about 4-5 times). Fig.S10 indicates that the CFB structures show an obvious catastrophic delamination, which significantly weakens structural integrity, and the experimental investigations are consistent with previous works (12). Further, Fig. S10*B* shows that an optimal pitch angle at which the fracture toughness reaches maximum in CFB structure does not exist any more, which can't explain why a specific pitch angle is so important in materials with Bouligand architectures. At a low pitch angle, the fracture energy of the DFB structure with discontinuous fibers is close to that in the CFB structure with continuous fibers, which is due to that the main crack propagated through the matrix without breaking any fiber in DFB and CFB structures. However, at a high pitch angle, the DFB structure show a crack-bridging mode, while the CFB structures show a catastrophic delamination. The fracture tests for our designed DFB structures show that the fracture toughness reaches maximum at a critical pitch angle, which is in good agreement with previous investigations for the critical pitch angle in natural materials with Bouligand structure. In the meanwhile, Fig. S4*D* and Fig. 5*B* shows that there also exists an optimal fiber length at which the fracture toughness reaches maximum in DFB structure, and the critical fiber length decreases with the increase of the pitch angle. The calculated results are consistent with the experimental results in Fig. 2*D* in the revised manuscript. Thus, the size effects of fibers are also very important to toughen the composite materials with Bouligand structure. Further, Fig. S11 shows that the flexural strength of DFB structure increases as the size of the fiber diameter decreases, which agrees with the scaling law of the mechanical properties of fibrous composites (13). Therefore, although the absolute values of the mechanical properties of the 3D-printed specimens in this work are not significant improvement due to the limitation of the spatial resolution of 3D-printing technology and available 3D-printing polymer materials, we believe that 3D-printing polymer materials with DFB structure down to nanoscale would achieve excellent fracture performance as predicted by our model, which provides the generic design strategies with parameters selection principle for the fabrication of

formidable fracture-resistant fibrous composite systems that adapt to loads in various in-plane orientations.

Table S1. The material parameters for 3D-printed DFB samples, the beetle's exoskeleton and twisted cellulose composites (6-10).

Materials	l	d	V_f	E	K_{Ic}^{f}	τ_m
3D-printed samples	20 mm	0.8 mm	0.7	0.8 GPa	184 $MPa \cdot mm^{1/2}$	0.1 MPa
beetle's exoskeleton	1 μm	20 nm	0.5	8 GPa	2 $MPa \cdot m^{1/2}$	10 MPa
Cellulose fibers	1 μm	10 nm	0.5	120 GPa	10 $MPa \cdot m^{1/2}$	20 MPa

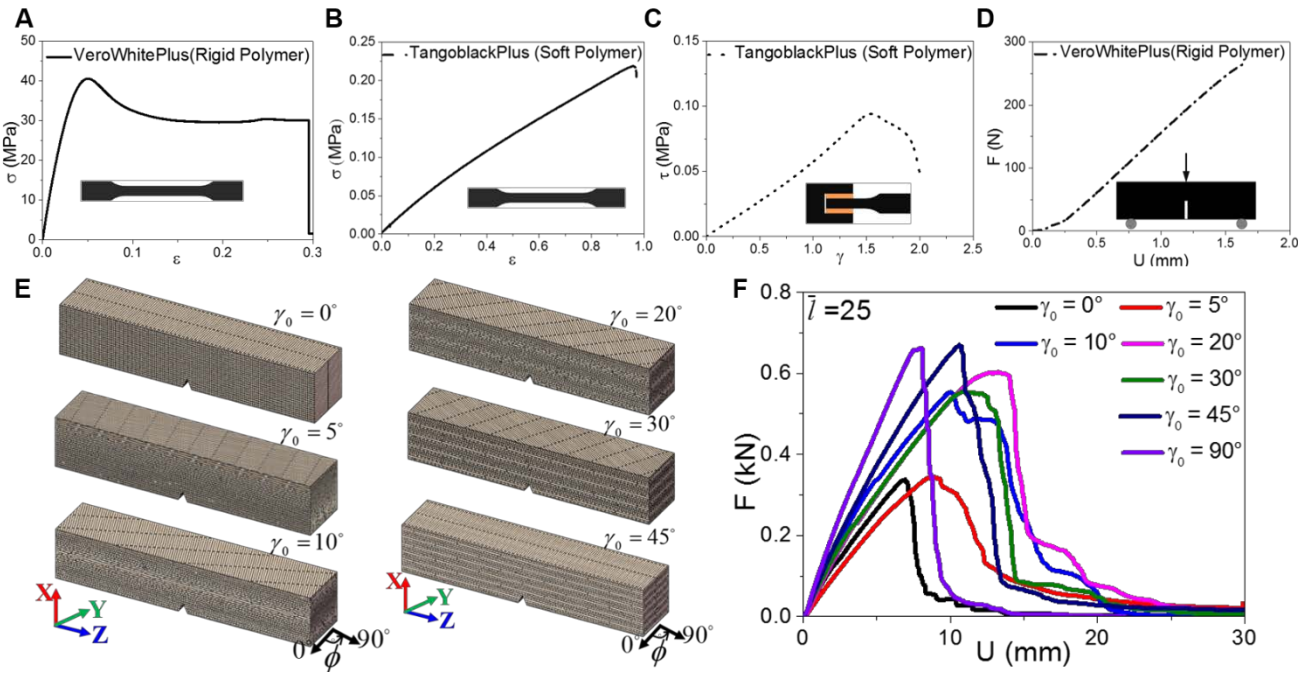

Fig. S1. Properties of composite constituents. Representative stress-strain curves for (*A*) Uniaxial tensile tests on pure fiber phase. (*B*) Uniaxial tensile tests on pure matrix phase. (***C***) Simple shear test on pure matrix phase. (*D*) Three-points bending tests on pure fiber phase. (*E*) Typical CAD models for the DFB composites under different pitch angles γ_0. (*F*) Representative force-displacement curves for 3D-printed samples of each pitch angle.

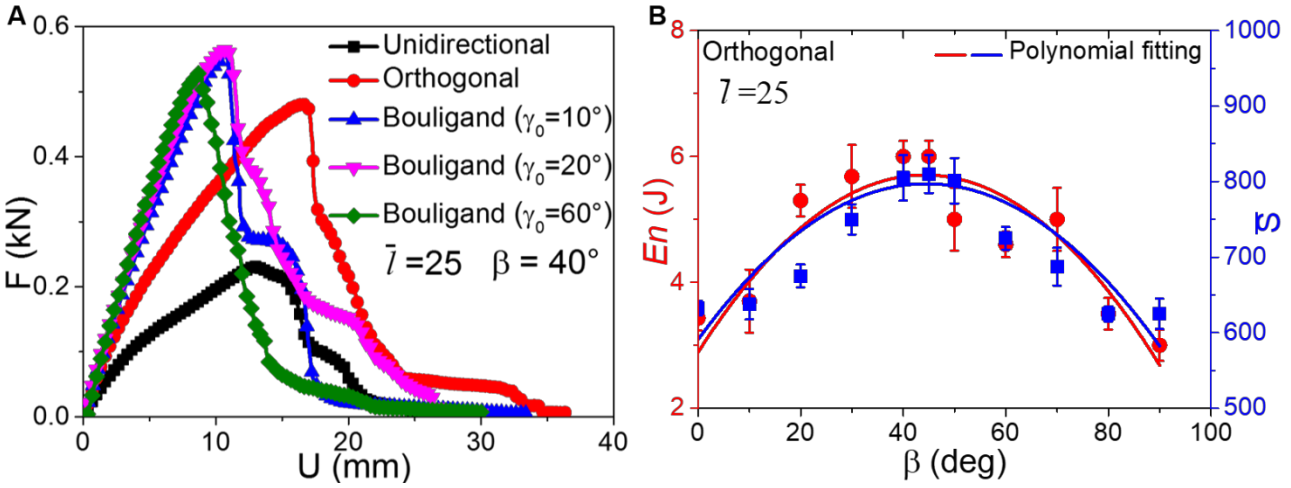

Fig. S2. Effects of initial crack orientations on frature performances. (*A*) Experimental force-displacement responses for different architectures (unidirectional, orthogonal and Bouligand structures) with $\beta = 40^\circ$ and $\bar{l} = 25$. (*B*) Effects of the orientation of initial crack tip β on the energy dissipation E_n and crack area $\bar{S} = S / d^2$ of the orthogonal architecture in experiments. Error bars represent one standard deviation measured over at least four samples .

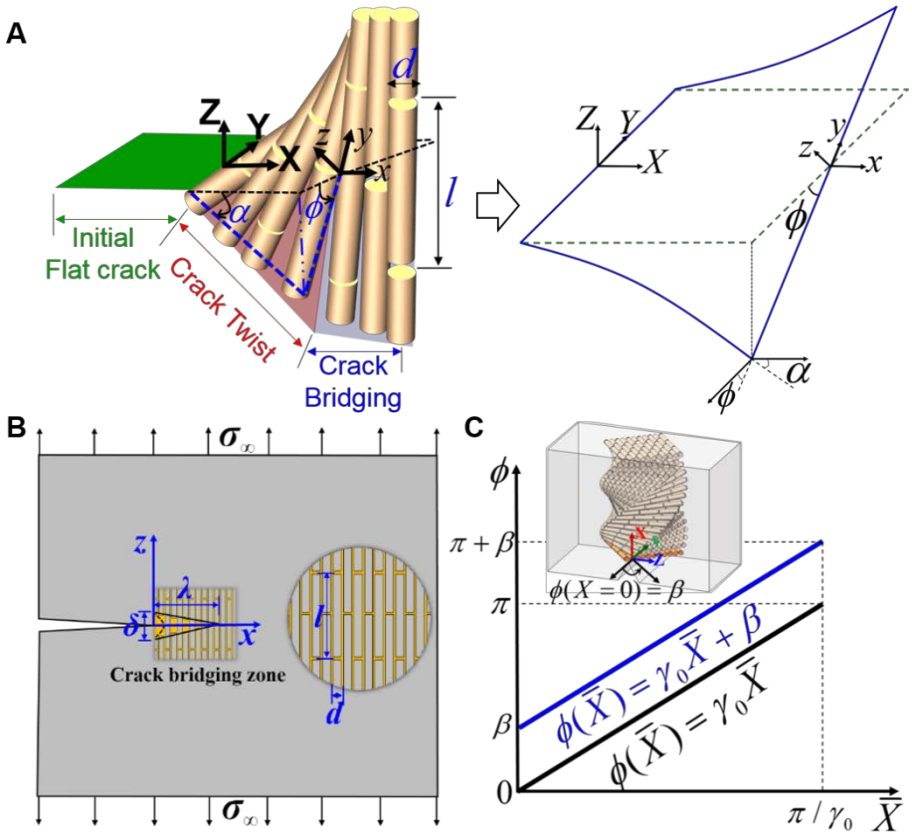

Fig. S3. Schematics for fracture mechanics model. (*A*) Schematic of a fracture mechanical model considering crack twisting and bridging simultaneously and a twisting surface. (*B*) Schematic of the crack-bridging model, where λ presents the bridging length and δ presents the crack opening displacement. (*C*) The distribution of twist angle ϕ ranges linearly from 0° to 180°, and the initial fibers layer at the notch tip orienting at $\phi=\beta$.

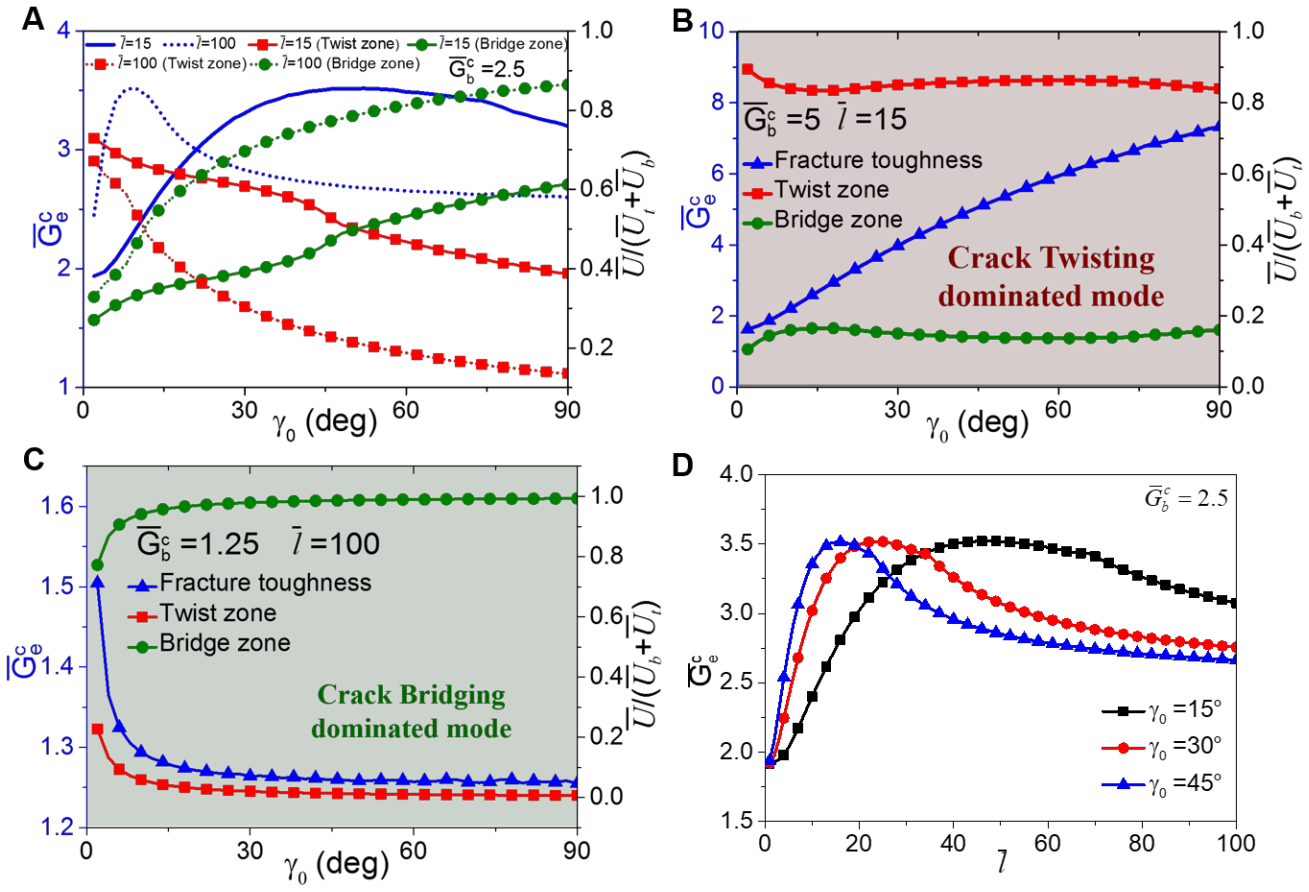

Fig. S4. Effects of structural parameters on effeactive fracture energy in DFB composite**s.** (*A*) Plots of the the effective fracture energy $\bar{G}_e^c$ and the proportions of released strain energy in crack twisting zone ($\bar{U}_t/\left(\bar{U}_t+\bar{U}_b\right)$) and crack bridging zone ($\bar{U}_b/\left(\bar{U}_t+\bar{U}_b\right)$) against pitch angles γ_0 for the structures with fiber length $\bar{l}=15$ and $\bar{l}=100$, respectively. Effects of γ_0 on $\bar{G}_e^c$, $\bar{U}_t/\left(\bar{U}_t+\bar{U}_b\right)$ and $\bar{U}_b/\left(\bar{U}_t+\bar{U}_b\right)$ in the structures (*B*) with $\bar{G}_b^c=5$, $\bar{l}=15$ and (*C*) with $\bar{G}_b^c=1.25$, $\bar{l}=100$. The background color in (*B*), (*C*) represents the dominated fracture modes including crack twisting (red) and crack bridging (green). (*D*) Effects of the dimensionless fiber length $\bar{l}$ on the effective fracture energy $\bar{G}_e^c$ in DFB structure with different pitch angle γ_0.

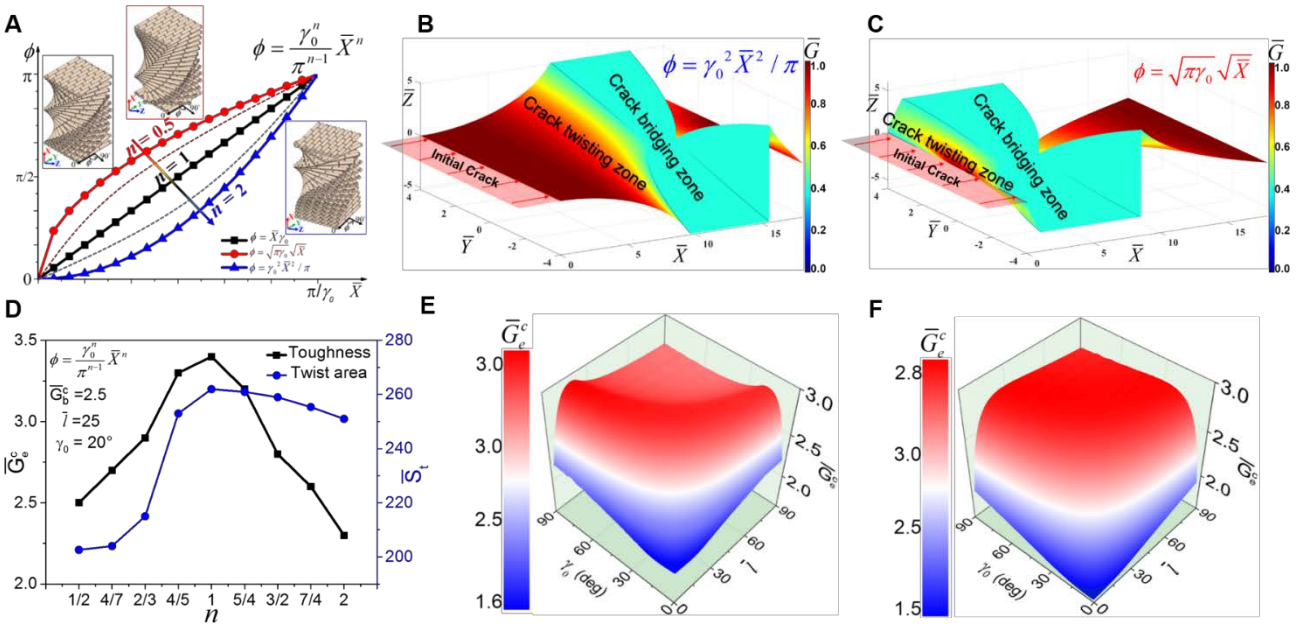

Fig. S5. Effects of the twist angles distribution on the fracture responses of the DFB structure. (*A*) The function of twist angle distribution ϕ in a rotation of 180°. The local energy release rate $\bar{G}$ and crack surface shape of structures with nonlinear twist angles distribution of (*B*) $\phi = \gamma_0^2 \bar{X}^2 / \pi$ and (*C*) $\phi = \sqrt{\pi\gamma_0}\sqrt{\bar{X}}$ when $\bar{l} = 8$, $\gamma_0 = 10^{\circ}$ and $\bar{G}_b^c = 2.5$. (*D*) Effects of twist angle distributions on the effective fracture energy $\bar{G}_e^c$ and the area of crack twisting zones $\bar{S}_t$. Plots for the optimized effective fracture energy depending on the pitch angles and fiber length in the structure under nonlinear twist angles distribution of (*E*) $\phi = \gamma_0^2 \bar{X}^2 / \pi$ and (*F*) $\phi = \sqrt{\pi\gamma_0}\sqrt{\bar{X}}$.

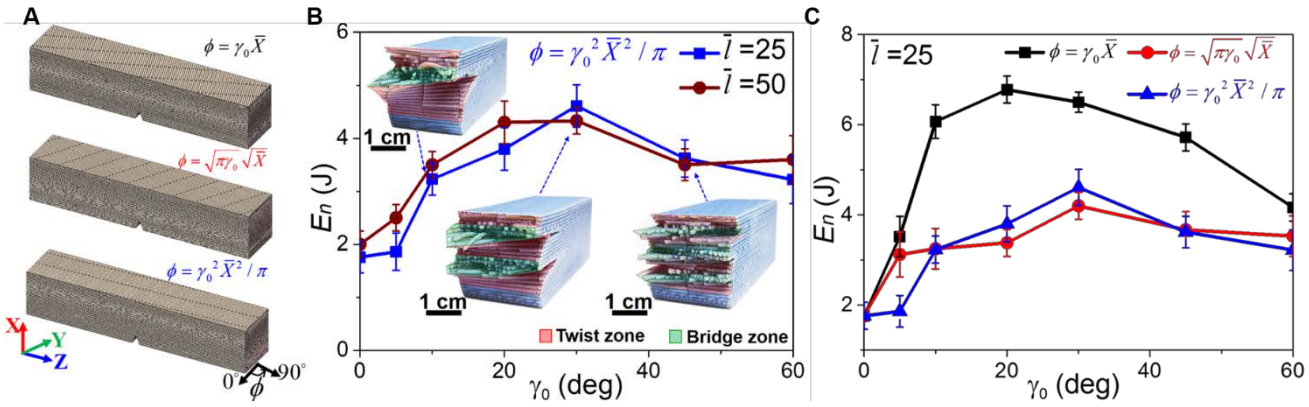

Fig. S6. Experimental investigations for the effects of twist angles distributions. (*A*) Typical CAD models for 3D-printed DFB composites with different twist angle distributions ϕ. (*B*) Effects of pitch angles γ_0 on the Energy dissipations E_n of the structure with different fiber lengths $\bar{l}$ under nonlinear twist angle distribution of $\phi=\gamma_0^2\bar{X}^2/\pi$. (*C*) E_n -γ_0 curves for the structures under different ϕ. Error bars in (*B*), (*C*) represent one standard deviation measured over at least 3 samples.

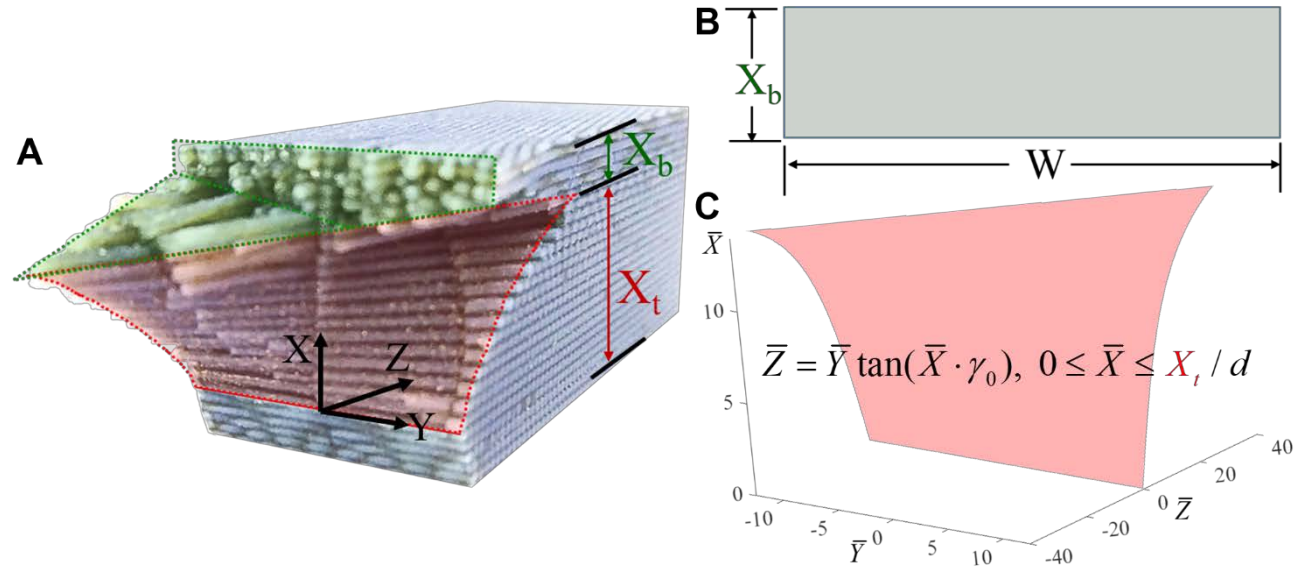

Fig. S7. (*A*) The fracture patterns composed of crack twisting zone (red) and crack bridging zone (green) in the DFB structure. (*B*) The profile of the crack bridging zone is fitted by a planar quadrilateral. (*C*) The profile of the crack bridging zone is characterized by an analytical equation.

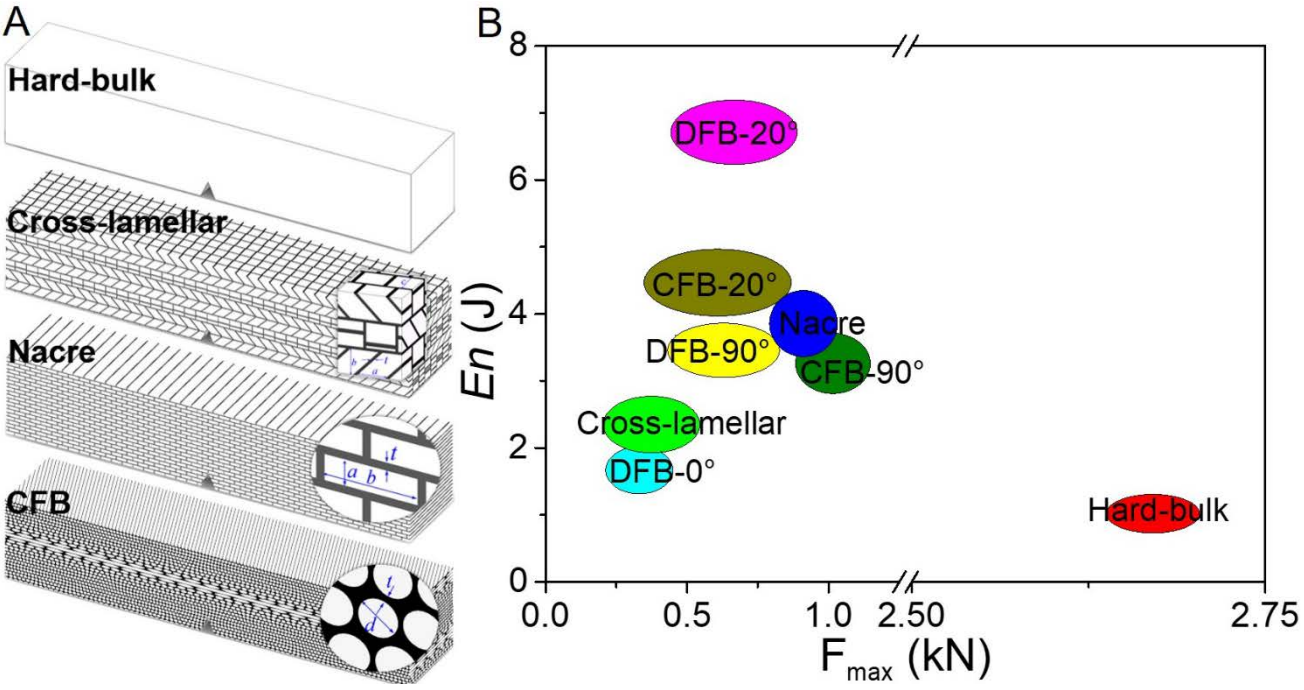

Fig. S8. (*A*) The geometric configurations for 3D-printed samples with four architectures, including the hard-bulk structure with stiff fiber phase, the cross-lamellar structure, the nacre-like structure, and the continuous fibrous Bouligand (CFB) structures. (*B*) Plots of the energy dissipation of fracture (*En*) versus the maximum force (F_{max}), illustrating a quantitative comparison between the discontinuous fibrous Bouligand (DFB) architecture and other four structures in (*A*).

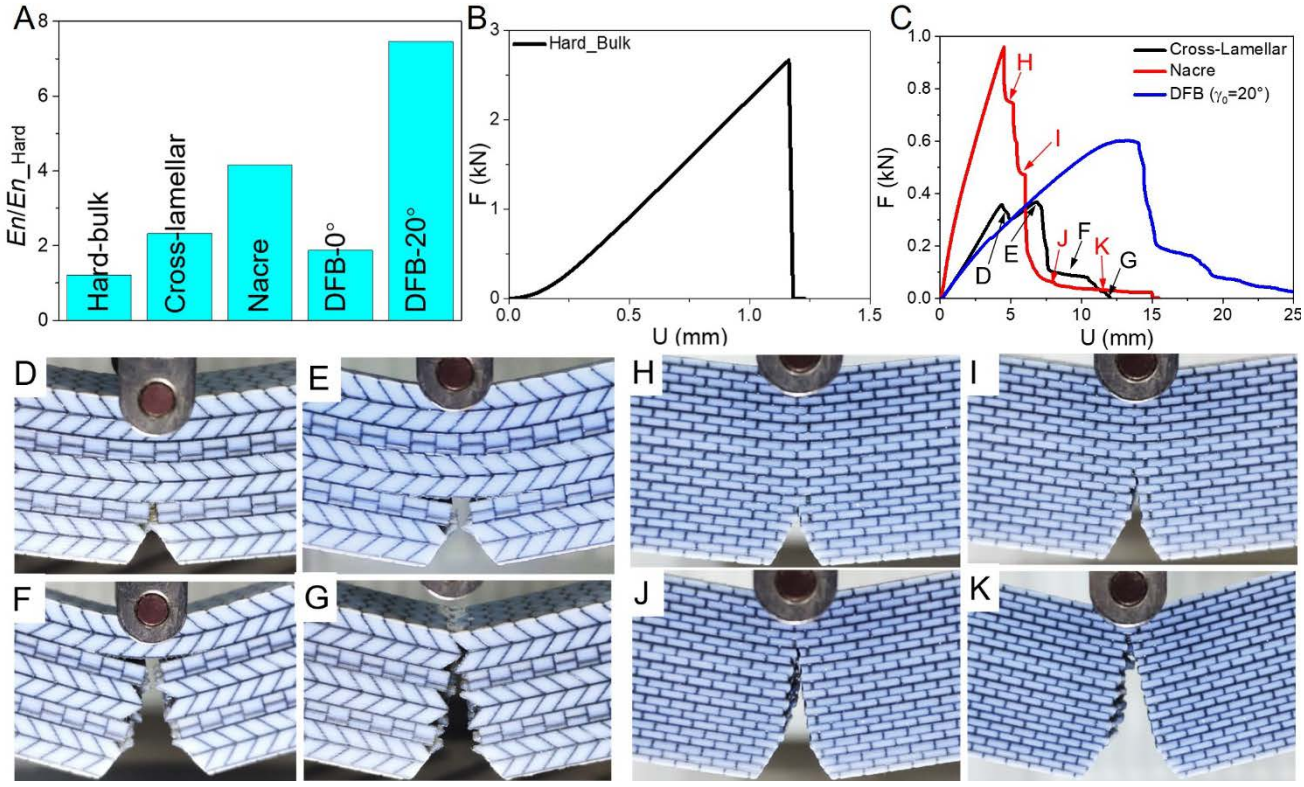

Fig. S9. (*A*) Fracture energy dissipation comparison between different architectures, including the

hard-bulk structure with stiff fiber phase, the cross-lamellar structure, the nacre-like structure, and the DFB structures with pitch angle of 0° (DFB-0°) and 20° (DFB-20°). (*B*) Force-displacement curve for the hard-bulk structure with stiff fiber phase. (*C*) Force-displacement curves for different architectures. (*D-G*) Crack propagation paths in the cross-lamellar structure. (*H-K*) Crack propagation paths in the nacre-like structure.

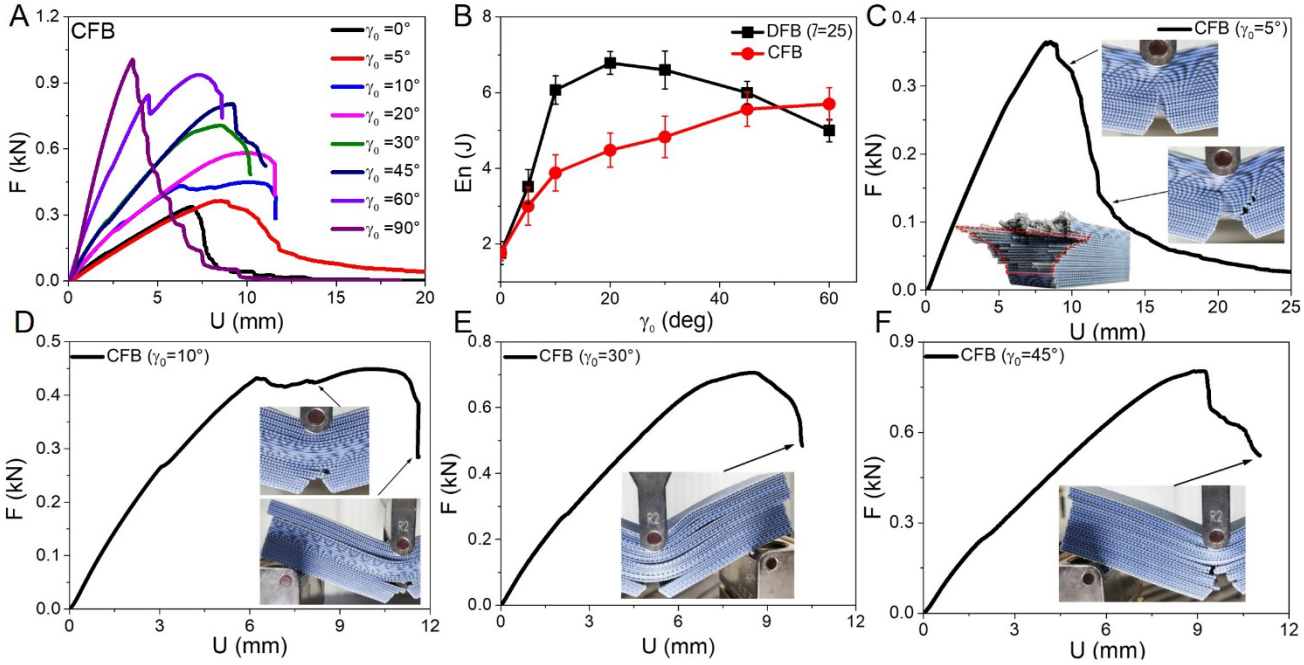

Fig. S10. (*A*) Force-displacement curves for the continuous fibrous Bouligand (CFB) structure with different pitch angles. (*B*) Fracture energy dissipation comparation between the DFB structure and the CFB structure under different pitch angles. (*C-F*) Crack propagation paths and delamination in the CFB structure with different pitch angles.

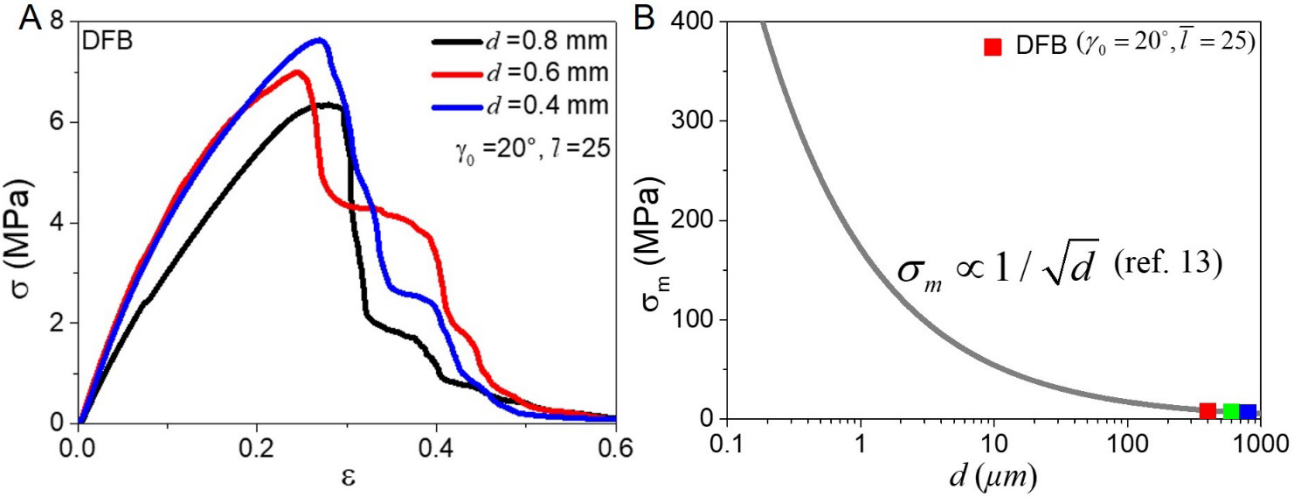

Fig. S11. (*A*) Flexural stress-strain curves for DFB structure with different fiber diameter *d*. (*B*)The

flexural strength σ_m tends to increase as the size of the internal architecture decreases, which is consistent with previous researches (13).

Supplementary References

1. K. T. Faber, A. G. Evans, Crack deflection processes—I. Theory. *Acta Metallurgica* **31**, 565-576 (1983).
2. N. Suksangpanya, N. A. Yaraghi, D. Kisailus, P. Zavattieri, Twisting cracks in Bouligand structures. *Journal of the Mechanical Behavior of Biomedical Materials* **76**, 38-57 (2017).
3. B. Budiansky, J. C. Amazigo, Toughening by aligned, frictionally constrained fibers. *Journal of the Mechanics and Physics of Solids* **37**, 93-109 (1989).
4. Y. Shao, H.-P. Zhao, X.-Q. Feng, H. Gao, Discontinuous crack-bridging model for fracture toughness analysis of nacre. *Journal of the Mechanics and Physics of Solids* **60**, 1400-1419 (2012).
5. Q. Meng, B. Li, T. Li, X.-Q. Feng, A multiscale crack-bridging model of cellulose nanopaper. *Journal of the Mechanics and Physics of Solids* **103**, 22-39 (2017).
6. R. Yang, A. Zaheri, W. Gao, C. Hayashi, H. D. Espinosa, AFM identification of beetle exocuticle: Bouligand structure and nanofiber anisotropic elastic properties. *Advanced Functional Materials* **27**, 1603993 (2017).
7. N. Ezekiel Mushi, N. Butchosa, Q. Zhou, L. A. Berglund, Nanopaper membranes from chitin–protein composite nanofibers—structure and mechanical properties. *Journal of Applied Polymer Science* **131**, 40124 (2014).
8. H. Gao, B. Ji, I. L. Jäger, E. Arzt, P. Fratzl, Materials become insensitive to flaws at nanoscale: lessons from nature. *Proceedings of the National Academy of Sciences* **100**, 5597-5600 (2003).
9. B. Natarajan et al., Binary cellulose nanocrystal blends for bioinspired damage tolerant photonic films. *Advanced Functional Materials* **28**, 1800032 (2018).
10. J. Song et al., Processing bulk natural wood into a high-performance structural material. *Nature* **554**, 224-228 (2018).
11. G. X. Gu, M. Takaffoli, M. J. Buehler, Hierarchically enhanced impact resistance of bioinspired composites, *Advanced Materials* **29**, 1700060 (2017).
12. N. Suksangpanya, N. A. Yaraghi, R. B. Pipes, D. Kisailus, P. Zavattieri, Crack twisting and toughening strategies in Bouligand architectures. *International Journal of Solids and Structures*

150, 83-106 (2018).

13. H. Zhu, et al. "Anomalous scaling law of strength and toughness of cellulose nanopaper." *Proceedings of the National Academy of Sciences* **112**, 8971-8976 (2015).